C6 Vol. 43, No. 7 / July 2026 / *Journal of the Optical Society of America A* **Research Article**

Journal of the Optical Society of America A
OPTICS, IMAGE SCIENCE, AND VISION

Correlated phase screens for beams in extreme turbulence

Liliana Borcea,[1,*] **Josselin Garnier,**[2,4] **and Knut Sølna**[3,5]

[1]Applied Physics and Applied Mathematics, Columbia University, New York, New York 10027, USA
[2]Centre de Mathématiques Appliquées, Ecole polytechnique, Institut Polytechnique de Paris, Palaiseau 91120, France
[3]Department of Mathematics, University of California at Irvine, Irvine, California 92697, USA
[4]josselin.garnier@polytechnique.edu
[5]ksolna@math.uci.edu
**lb3539@columbia.edu*

Received 5 January 2026; revised 21 March 2026; accepted 22 March 2026; posted 23 March 2026; published 13 April 2026

Beam propagation through turbulence is commonly simulated by split-step Fourier methods with independent phase screens. This approach relies on the paraxial-Markov approximation, which has a wide range of validity. However, it is not justified in strongly turbulent media, where correlated phase screens are needed. Examples of extreme turbulence, considered in the paper, arise, for example, in beam propagation through a jet plume and in aero-optics applications. The goal of this paper is two-fold: first, it clarifies when the use of independent phase screens fails, meaning that it corrupts the estimated statistics of the wave field. Second, it describes an efficient method for sampling correlated phase screens, denoted by the acronym SCE-DFT. It uses the discrete fast Fourier transform and circulant embedding, with a particular spline-based smooth embedding, designed to improve the efficiency.

https://doi.org/10.1364/JOSAA.589339

1. INTRODUCTION

The quantification of loss of coherence, beam wander, and scintillation of laser beams propagating through atmospheric turbulence is important for understanding limitations and performance degradation of LIDAR, laser-guided systems, and free-space optical communication. It is the topic of numerous studies of beam propagation through random media, where the randomness models the uncertainty of the fluctuating index of refraction [1–3]. Roughly, there are two types of theories: weak-fluctuation (perturbative) ones like the Born and Rytov approximations ([1], Chapter 5) and the strong fluctuation ones governed by the paraxial wave equation ([1], Chapter 7). We are interested in strong turbulence, so we consider the paraxial wave model.

In the orthogonal system of coordinates $\vec{\boldsymbol{x}} = (\boldsymbol{x}, z) \in \mathbb{R}^{d+1}$, with range axis z, the beam is modeled by the wave field:

$$u(\vec{\boldsymbol{x}}) = e^{ikz}\psi(\vec{\boldsymbol{x}}), \tag{1}$$

with homogeneous wave number k. Here, e^{ikz} is a rapidly oscillating plane wave propagating in the range direction, and $\psi(\vec{\boldsymbol{x}})$ is the slowly varying envelope of the beam, satisfying the paraxial wave equation [1,3–6]

$$\partial_z \psi(\vec{\boldsymbol{x}}) = \frac{i}{2k}\Delta_{\boldsymbol{x}}\psi(\vec{\boldsymbol{x}}) + \frac{ik}{2}\mu(\vec{\boldsymbol{x}})\psi(\vec{\boldsymbol{x}}), \quad \vec{\boldsymbol{x}} = (\boldsymbol{x}, z) \in \mathbb{R}^d \times \mathbb{R}_+,$$
$$\psi(\boldsymbol{x}, z = 0) = \psi_0(\boldsymbol{x}), \tag{2}$$

with random fluctuations $\mu(\vec{\boldsymbol{x}})$ of the squared index of refraction $n^2(\vec{\boldsymbol{x}})$ (i.e., $\mu(\vec{\boldsymbol{x}}) = n^2(\vec{\boldsymbol{x}})/n_o^2 - 1$ with $n_o^2 = \mathbb{E}[n^2(\vec{\boldsymbol{x}})]$ the homogeneous squared index of refraction). A generic model of these fluctuations is a mean zero, stationary, and isotropic Gaussian random process with power spectral density:

$$\mathbb{S}(\vec{\boldsymbol{\kappa}}) = \int_{\mathbb{R}^{d+1}} \mathbb{E}\left[\mu(\vec{\boldsymbol{x}}')\mu(\vec{\boldsymbol{x}}' + \vec{\boldsymbol{x}})\right] e^{-i\vec{\boldsymbol{\kappa}}\cdot\vec{\boldsymbol{x}}} \mathrm{d}\vec{\boldsymbol{x}}$$
$$= \chi_\alpha \mathbf{1}_{(L_o^{-1}, l_o^{-1})}(|\vec{\boldsymbol{\kappa}}|)|\vec{\boldsymbol{\kappa}}|^{-d-\alpha}, \tag{3}$$

where the expectation is with respect to the Gaussian measure. In this model, χ_α is a constant parameterized by $\alpha \in (0, 2)$, the length scales L_o and l_o are ordered as $0 < l_o < L_o$, and we denote by $\mathbf{1}_{(L_o^{-1}, l_o^{-1})}(|\vec{\boldsymbol{\kappa}}|)$ the indicator function equal to one when $|\vec{\boldsymbol{\kappa}}| \in (L_o^{-1}, l_o^{-1})$ and zero otherwise.

Definition (3) is a generalization of the Kolmogorov power law spectrum ([1], Chapter 3), where $\alpha = 5/3$, and L_o and l_o are the outer and inner scales of turbulence. The covariance of $\mu(\vec{\boldsymbol{x}})$ is the inverse Fourier transform of (3). It has the isotropic expression

1084-7529/26/0700C6-14 Journal © 2026 Optica Publishing Group

$$\mathbb{E}\left[\mu(\vec{\boldsymbol{x}}')\mu(\vec{\boldsymbol{x}}'+\vec{\boldsymbol{x}})\right] = R_d(|\vec{\boldsymbol{x}}|) = \frac{\chi_\alpha |\vec{\boldsymbol{x}}|^{\alpha-1}}{2\pi^d} \times \begin{cases} \displaystyle\int_{|\vec{\boldsymbol{x}}|/L_o}^{|\vec{\boldsymbol{x}}|/l_o} s^{-\alpha}\,\mathrm{sinc}(s)\mathrm{d}s\,, & \text{if } d=2, \\ \displaystyle\int_{|\vec{\boldsymbol{x}}|/L_o}^{|\vec{\boldsymbol{x}}|/l_o} s^{-\alpha} J_0(s)\mathrm{d}s\,, & \text{if } d=1, \end{cases} \tag{4}$$

whose limit as $|\vec{\boldsymbol{x}}| \to 0$ gives the variance

$$\mathbb{E}\left[\mu^2(\vec{\boldsymbol{x}}')\right] = R_d(0) = \frac{\chi_\alpha}{2\pi^d}\int_{L_o^{-1}}^{l_o^{-1}} \kappa^{-\alpha}\mathrm{d}\kappa$$

$$= \begin{cases} \frac{\chi_\alpha}{2\pi^d}\left(\frac{L_o^{\alpha-1}-l_o^{\alpha-1}}{\alpha-1}\right), & \text{if } \alpha \in (0,\,1)\cup(1,\,2), \\ \frac{\chi_1}{(2\pi^d)}\ln(L_o/l_o), & \text{if } \alpha = 1. \end{cases} \tag{5}$$

Most beam propagation studies are for $\alpha > 1$, which makes $R_d(|\vec{\boldsymbol{x}}|)$ integrable. The mathematical implication is that $\psi(\vec{\boldsymbol{x}})$ is described asymptotically by the solution of an Itô-Schrödinger equation driven by a Brownian field with covariance defined in terms of $\mathbb{S}(\vec{\boldsymbol{\kappa}})$ [6]. The asymptotics is in the high frequency limit, for various scalings of the radius of support of the initial condition $\psi_o(\boldsymbol{x})$ and ranges of propagation, where phenomena like beam wander (spot-dancing) [7] and scintillation (strong intensity fluctuations that have Gaussian statistics) [8,9] have been characterized in detail. The covariance $s \mapsto R_d(s)$ is not integrable in the case $\alpha < 1$ and $L_o = +\infty$, so the process $\mu(\vec{\boldsymbol{x}})$ has long-range correlation [10]. This case is relevant in cloudy atmosphere [11,12], and the randomization of the beam has a less understood and more complicated multi-scale characterization [13,10,14].

In optics applications, the measured quantity is the intensity $|\psi(\vec{\boldsymbol{x}})|^2$, whose random fluctuations are described by fourth-order statistical moments. Most of the existing mathematical analysis characterizes the first two moments of $\psi(\vec{\boldsymbol{x}})$, the mean and the covariance. Access to the fourth- or higher-order moments of $\psi(\vec{\boldsymbol{x}})$ is limited to simpler regimes, like in a scintillation regime [8,9], where $\psi(\vec{\boldsymbol{x}})$ has Gaussian statistics and Isserlis's theorem applies [15]. However, $\psi(\vec{\boldsymbol{x}})$ is not Gaussian in general regimes. For example, the analysis in [7,16,17] shows that in the spot-dancing regime, which describes beam wander, the intensity has a Rice–Nakagami statistics. The theoretical analysis of higher-order moments of $\psi(\vec{\boldsymbol{x}})$ remains out of reach in general regimes. This motivates the empirical estimation of the moments via Monte Carlo numerical simulations.

Split-step Fourier methods [18–21] approximate the solution $\psi(\vec{\boldsymbol{x}})$ of (2) by alternating between two simplifications, in successive range intervals Δz that discretize the range coordinate: the first simplification accounts only for the diffraction component. It neglects the random term $\frac{ik}{2}\mu(\vec{\boldsymbol{x}})\psi(\vec{\boldsymbol{x}})$ and solves the resulting deterministic paraxial wave equation using the Fourier transform. The second simplification neglects the diffraction term $\frac{i}{2k}\Delta_{\boldsymbol{x}}\psi(\vec{\boldsymbol{x}})$ and integrates the resulting equation to obtain a random phase aka, a phase screen. There is a trade-off between the accuracy and computational cost of split-step methods that is controlled by the discretization step Δz. On one hand, Δz should be small enough to get an accurate solution [4,18,22]. On the other hand, the generation of the phase screens is simpler if Δz is larger than the outer scale L_o. Then, a Markov approximation allows the use of statistically uncorrelated screens [22].

We show in this paper that in many cases, it is possible to choose a Δz that satisfies this accuracy versus efficiency trade-off. However, in media with long-range correlations of $\mu(\vec{\boldsymbol{x}})$ [23], or in regimes of extreme turbulence, the two requirements on Δz may not be reconciled, and one needs to use correlated phase screens. Such extreme turbulence arises, for example, in laser beam propagation through jet engine plume environments [24,25], where significant beam wander, scintillation, and broadening have been reported [26,27]. We illustrate this regime for the model (3) by choosing parameters similar to those in [28]. Other examples of extreme turbulence can be found in aero-optics [29–32], where atmosphere (fluid) displacement in the path of laser carrying, high-speed aircraft causes non-negligible density variations and significant pressure drops [30,31]. It is not easy to draw a connection between the generic model (3) of turbulence and those relevant to aero-optics applications. The models there depend strongly on the aerodynamic environment (shape/size of the aircraft) and the quantification of the fluid-optic interactions is not fully understood [29]. Nevertheless, we make a choice of the parameters in (3) that could be relevant for aero-optics.

Monte Carlo simulations require the generation of a very large number of realizations of the correlated phase screens, on a discrete grid of $n+1$ points in a set Ω. If we denote by $\mathbf{Y}$ the $(n+1)$-dimensional column vector of phase screen samples at the grid points, the task is to generate many realizations of $\mathbf{Y}$, given knowledge of the covariance matrix $\mathscr{C} = \mathbb{E}[\mathbf{Y}\mathbf{Y}^T]$, where the superscript T denotes the transpose. This is a symmetric and positive definite matrix, with entries defined in terms of $R_d(|\vec{\boldsymbol{x}}|)$, as explained later in the paper. One approach for generating $\mathbf{Y}$ is to take a square-root factorization of the covariance $\mathscr{C} = \boldsymbol{\Gamma}\boldsymbol{\Gamma}^T$ and then define $\mathbf{Y} = \boldsymbol{\Gamma}\boldsymbol{\eta}$, where $\boldsymbol{\eta} \sim \mathcal{N}(0, \mathbf{I})$ is a standard Gaussian n-dimensional random vector. The ensemble of generated vectors $\mathbf{Y}$ has the exact covariance

$$\mathbb{E}[\mathbf{Y}\mathbf{Y}^T] = \boldsymbol{\Gamma}\mathbb{E}[\boldsymbol{\eta}\boldsymbol{\eta}^T]\boldsymbol{\Gamma}^T = \boldsymbol{\Gamma}\boldsymbol{\Gamma}^T = \mathscr{C},$$

but the problem is that the $O(n^3)$ computational cost of the square-root $\boldsymbol{\Gamma}$ is prohibitively expensive in more than one dimension, because the number $n+1$ of grid points is too large. This has motivated the use of spectral methods that are efficient, because they use the fast Fourier transform (FFT), but produce vectors $\mathbf{Y}$ that do not have the exact covariance [33]. Several improvements of the FFT-based approach have been introduced in [20,34,35]. They involve truncated trigonometric series with carefully chosen random amplitudes and phases, and they can be efficient even with a limited number of modes. Moreover, unlike the standard FFT methods, they can produce samples on general (non-regular) grids. The covariance of these samples is still, however, an approximation of the desired one. It is difficult to quantify theoretically the error of the approximation, but the methods have been validated by numerical simulations carried out for some popular turbulence models in [20,35].

In this paper, we generate the phase screens on a rectangular grid Ω using an original extension of the circulant embedding approach introduced in [36], and used for phase screen generation, for instance, in [37]. Our method is denoted by the acronym SCE-DFT (smooth circulant embedding-discrete Fourier transform). Its computational cost and memory requirement are similar to those of FFT methods, i.e., $O(n \log n)$ flops and $O(n)$, respectively. The generated samples have either the exact covariance or very good approximations of it, with theoretically quantifiable error. SCE-DFT benefits from the computational efficiency of the FFT method. It circumvents the limitations of the classical FFT approach, in that it does not produce periodic samples but samples with the exact distribution (or quasi-exact distribution, with explicit error bounds). The low-frequency part of the turbulence spectrum is well represented as a consequence of the control of the distribution and, although the grid is regular, it is possible to choose the spatial and spectral domain sizes and resolutions independently.

In some applications, one may be interested in a local grid refinement, which makes the overall grid irregular. We do not consider refinements in this paper, but remark that they can be carried out efficiently, in a second step following the SCE-DFT, via conditional Gaussian sampling or Kriging ([38], Section 7.3). The conditioning is done on a neighborhood of grid points on the regular grid. This exploits a quasi-Markovian property in that this neighborhood effectively shields the effects of remote grid points on the regular grid. The locally irregular grids due to refinement do not allow the use of FFT. However, in applications, the number of refinement and conditioning nodes is expected to be much smaller than the size of the original regular grid. Therefore, they can be dealt with using direct factorization (Cholesky) methods.

The goal of the paper is two-fold: first, we clarify in which scaling regimes the paraxial-Markov approximation with uncorrelated phase screens may fail and also quantify the subsequent distortion of the estimated moments of $\psi(\vec{\boldsymbol{x}})$. Second, we show that the SCE-DFT method can be implemented efficiently for beam propagation through extreme turbulence. The original circulant embedding method introduced in [36] is guaranteed to generate ensembles of vectors with the exact covariance matrix $\mathscr{C}$, if the grid Ω is embedded in a large enough d-dimensional cuboid [39]. The large cuboid makes circulant embedding computationally expensive. Our SCE-DFT approach shows that, in fact, it is possible to work with much smaller cuboids by using an appropriate, smooth embedding at the expense of a small and theoretically quantifiable error of the approximation of $\mathscr{C}$. This makes the SCE-DFT method both theoretically guaranteed and numerically efficient.

The paper is organized as follows: we begin in Section 2 with the split-step Fourier method, the definition of the phase screens, and the discussion of the validity of the paraxial-Markov approximation. In Section 3, we describe the SCE-DFT approach for generating correlated phase screens and quantify how the size of the embedding cuboid affects its accuracy. The simulation results are presented in Section 4, where we compare the estimated moments with the uncorrelated and the correlated phase screens. We present some conclusions in Section 5. In Appendix C, we use a typical example to illustrate how the SCE-DFT method significantly outperforms the classic version of circulant embedding with a smooth pasting to zero.

2. PHASE SCREEN METHOD

In this section, we review the split-step Fourier approximation of the solution of the paraxial Eq. (2) and describe the statistics of the phase screens, for the random process with power spectral density (3). Then, we study the regime of validity of the Markov approximation, where the phase screens are considered statistically independent. We end with the motivation of using correlated phase screens for beam propagation through very strong turbulence.

A. Split-Step Fourier Approximation

Suppose that we wish to compute the solution $\psi(\vec{\boldsymbol{x}})$ of (2), at $\vec{\boldsymbol{x}} = (\boldsymbol{x}, Z)$, where Z denotes the total, long range of propagation. The split-step (phase screen) method [40] divides the range Z into n subintervals (z_j, z_{j+1}) of length Δz, with $z_j = j\Delta z$, for $j = 0, \ldots, n_z$ and $\Delta z = Z/n_z$. In each subinterval, the beam is evolved approximately by solving two simpler equations in sequence:

1. The first equation takes into account the deterministic diffraction component

$$\partial_z \phi(\boldsymbol{x}, z) = \frac{i}{2k} \Delta_{\boldsymbol{x}} \phi(\boldsymbol{x}, z), \quad z \in (z_j, z_{j+1}), \tag{6}$$

starting from $\phi(\boldsymbol{x}, z_j) = \phi_j(\boldsymbol{x})$. Its solution at the end of the interval is

$$\phi_{j+1}(\boldsymbol{x}) = \phi(\boldsymbol{x}, z_{j+1}) = [\mathcal{A}(z_{j+1}, z_j)\phi_j](\boldsymbol{x}), \tag{7}$$

with the operator

$$[\mathcal{A}(z_{j+1}, z_j)\phi_j](\boldsymbol{x}) = \frac{1}{(2\pi)^d} \int_{\mathbb{R}^d} [\mathcal{F}\phi_j](\boldsymbol{\kappa}) \times \exp\left(-i\frac{|\boldsymbol{\kappa}|^2 (z_{j+1} - z_j)}{2k} + i\boldsymbol{\kappa} \cdot \boldsymbol{x}\right) \mathrm{d}\boldsymbol{\kappa}, \tag{8}$$

defined using the Fourier transform

$$[\mathcal{F}\phi_j](\boldsymbol{\kappa}) = \hat{\phi}_j(\boldsymbol{\kappa}) = \int_{\mathbb{R}^d} \phi_j(\boldsymbol{x}) \exp(-i\boldsymbol{\kappa} \cdot \boldsymbol{x}) \mathrm{d}\boldsymbol{x}. \tag{9}$$

2. The second equation takes into account the random phase modulation

$$\partial_z \phi(\boldsymbol{x}, z) = \frac{i}{2k} \mu(\boldsymbol{x}, z) \phi(\boldsymbol{x}, z), \quad z \in (z_j, z_{j+1}), \tag{10}$$

starting from $\phi(\boldsymbol{x}, z_j) = \phi_j(\boldsymbol{x})$, and its solution at the end of the subinterval is

$$\phi_{j+1}(\boldsymbol{x}) = \phi(\boldsymbol{x}, z_{j+1}) = [\mathcal{B}(z_{j+1}, z_j)\phi_j](\boldsymbol{x}), \tag{11}$$

with the operator

$$[\mathcal{B}(z_{j+1}, z_j)\phi_j](\boldsymbol{x}) = \exp\left(\frac{ik}{2} \int_{z_j}^{z_{j+1}} \mu(\boldsymbol{x}, z) \mathrm{d}z\right) \phi_j(\boldsymbol{x}). \tag{12}$$

The integral that defines the random phase in this equation is called a phase screen.

The result after n_z steps is

$$\psi(\boldsymbol{x}, Z) \approx \left[\prod_{j=0}^{n_z-1} \mathcal{B}(z_{j+1}, z_j)\mathcal{A}(z_{j+1}, z_j) \right] \psi_0(\boldsymbol{x}). \tag{13}$$

It is only an approximation of $\psi(\boldsymbol{x}, Z)$ because the evolution operators (8) and (12) do not commute. This approximation improves as Δz decreases, as shown by the convergence analysis results in [4,18,19,23].

Another version of split-stepping is given by Strang's method [41,42], which takes half a step using the operator $\mathcal{A}$, then takes a full step with the operator $\mathcal{B}$, and then takes a second half step again with $\mathcal{A}$. Note from the definition (8) that $\mathcal{A}$ is translation invariant:

$$\begin{aligned} &\mathcal{A}(z_{k+1/2}, z_{k-1/2}) \\ &= \mathcal{A}(z_k, z_{k-1}) = \mathcal{A}(z_1, z_0), \quad \text{for all } k = 1, \ldots, n_z - 1, \end{aligned}$$

and that

$$\mathcal{A}(z_{k+1/2}, z_{k-1/2}) = \mathcal{A}(z_{k+1/2}, z_k)\mathcal{A}(z_k, z_{k-1/2}).$$

This implies that the Strang scheme differs from (13) just in the first and last steps [43]:

$$\begin{aligned} \psi(\boldsymbol{x}, Z) \approx \big[&\mathcal{A}(z_{n_z}, z_{n_z-1/2})\mathcal{B}(z_{n_z}, z_{n_z-1})\mathcal{A}(z_{n_z-1}, z_{n_z-2}) \cdots \\ &\cdots \mathcal{A}(z_2, z_1)\mathcal{B}(z_1, z_0)\mathcal{A}(z_{1/2}, z_0)\psi_0\big](\boldsymbol{x}). \end{aligned} \tag{14}$$

The computational burden in the split-step algorithm is the repeated direct and inverse Fourier transforms that define the operators $\mathcal{A}$ and the generation of the random phase screens that define the operators $\mathcal{B}$. The fast Fourier transform (FFT) can obviously be used for the computation of $\mathcal{A}$. Moreover, when combined with the circulant embedding approach [36], it gives an efficient and accurate computation of the phase screens that define the operator $\mathcal{B}$ (see Section 3).

B. Statistics of the Phase Screens

The phase screen at the jth step is defined by

$$U_j(\boldsymbol{x}) = \int_{j\Delta z}^{(j+1)\Delta z} \mu(\boldsymbol{x}, z)\mathrm{d}z, \quad \boldsymbol{x} \in \mathbb{R}^d, \; j = 0, \ldots, n_z - 1. \tag{15}$$

It is a Gaussian process (since $\mu(\vec{\boldsymbol{x}})$ is assumed Gaussian) that is stationary in $(j, \boldsymbol{x})$ with mean zero. Its covariance is derived in Appendix A, and it is described next.

- The covariance of the phase screens is given by

$$\begin{aligned} &\mathbb{E}[U_{j'+j}(\boldsymbol{x}' + \boldsymbol{x})U_{j'}(\boldsymbol{x}')] = \mathbb{E}[U_j(\boldsymbol{x})U_0(\mathbf{0})] \\ &= \int_{(j-1)\Delta z}^{j\Delta z} [s - (j-1)\Delta z] R_d(|(\boldsymbol{x}, s)|)\mathrm{d}s \\ &\quad + \int_{j\Delta z}^{(j+1)\Delta z} [(j+1)\Delta z - s] R_d(|(\boldsymbol{x}, s)|)\mathrm{d}s, \end{aligned} \tag{16}$$

with R_d defined in (4) and $d \in \{1, 2\}$.

- The variance of the phase screens is given by

$$\mathbb{E}[U_0(\mathbf{0})^2] = \frac{\chi_\alpha \Delta z^{1+\alpha}}{\pi^d \alpha} \Psi_d\left(\frac{\Delta z}{L_o}, \frac{\Delta z}{l_o}\right), \tag{17}$$

$$\Psi_d(s_1, s_2) = \begin{cases} \displaystyle\int_0^{s_2} \operatorname{sinc}(u) P(u, s_1, s_2)\mathrm{d}u, & \text{if } d = 2, \\ \displaystyle\int_0^{s_2} J_0(u) P(u, s_1, s_2)\mathrm{d}u, & \text{if } d = 1, \end{cases} \tag{18}$$

with J_0 as the Bessel function of the first kind of order zero, and with

$$\begin{aligned} P(u, s_1, s_2) = (u \vee s_1)^{-\alpha} - s_2^{-\alpha} - \frac{\alpha u}{\alpha + 1}(u \vee s_1)^{-\alpha-1} \\ + \frac{\alpha u}{\alpha + 1} s_2^{-\alpha-1}. \end{aligned} \tag{19}$$

The notation $u \vee s_1$ stands for $\max\{u, s_1\}$.

- When $\Delta z \gg L_o > l_o$, we have, for $d \in \{1, 2\}$

$$\mathbb{E}[U_0(\mathbf{0})^2] = \frac{\chi_\alpha (L_o^\alpha - l_o^\alpha)}{d\pi\alpha}[\Delta z + o(\Delta z)], \tag{20}$$

$$\mathbb{E}[U_n(\boldsymbol{x})U_0(\mathbf{0})] = \left(\chi_\alpha L_o^\alpha\right) o(\Delta z), \quad \text{if } n \neq 0, \tag{21}$$

and

$$\begin{aligned} \mathbb{E}[U_0(\boldsymbol{x})U_0(\mathbf{0})] &= \frac{1}{(2\pi)^d} \int_{\mathbb{R}^d} \mathbb{S}(\boldsymbol{\kappa}, 0)e^{-i\boldsymbol{\kappa}\cdot\boldsymbol{x}}\mathrm{d}\boldsymbol{\kappa}[\Delta z + o(\Delta z)] \\ &= \frac{\chi_\alpha}{d\pi} \int_{L_o^{-1}}^{l_o^{-1}} s^{-1-\alpha} Q_d(s|\boldsymbol{x}|)\mathrm{d}s[\Delta z + o(\Delta z)], \end{aligned} \tag{22}$$

with $Q_1(r) = \cos(r)$, $Q_2(r) = J_0(r)$, and $o(\Delta z)$ denoting a length scale satisfying $o(\Delta z)/\Delta z \to 0$ as $\Delta z \to 0$.

C. Validity of the Markov Approximation

Equations (21) and (22) with the $o(\Delta z)$ terms neglected give the covariance of the phase screens used in the optics literature ([1], Eq. (14), Section 15.2.1). As from Eqs. (16)–(22), it is an approximation of the covariance (16), derived in the asymptotic regime $\Delta z \gg L_o > l_o$. In general, the phase screens are correlated. It is only for $\Delta z \gg L_o$ that the correlation of the screens becomes negligible, per equation (21). Since the phase screens are Gaussian distributed, this implies that the phase screens are independent.

We conclude from Sections 2.A and 2.B that the discretization step Δz must satisfy a trade-off, in order for the split-step Fourier method with independent phase screens to give accurate estimates of the statistics of $\psi(\vec{\boldsymbol{x}})$:

(H1) On one hand, Δz must be much larger than L_o, so that the Markov approximation (independent of the phase screens) can be used. For example, in [44], it is stated that the phase screen can be assumed independent when $\Delta z / L_o \geq 5$.

(H2) On the other hand, Δz must be small enough for the split step approximations (13) or (14) to be accurate [18,19]. For example, in [22], it is required that the change of $|\psi(\vec{\boldsymbol{x}})|$ over a step Δz be less than 5%.

There are different versions of the hypothesis (H2) in the literature. We cite some of them, for $d = 2$, i.e., propagation in three dimensions, and for the Kolmogorov spectrum. It is stated in ([1, Eq. (20), Section 8.2) that for a plane wave propagating over the range interval Δz, and under the assumption that the intensity perturbation is weak, the intensity variance is approximated by the Rytov formula:

$$\sigma_R^2 = 1.23 C_n^2 k^{7/6} \Delta z^{11/6}. \tag{23}$$

In [45], the authors require that σ_R^2 be smaller than some threshold, typically 0.05^2, which gives a criterium of the form

$$\begin{aligned} \Delta z &< k^{-7/11} (C_n^2)^{-6/11} (0.05^2/1.23)^{6/11} \\ &= 0.034 k^{-7/11} (C_n^2)^{-6/11}. \end{aligned} \tag{24}$$

In [28,46], it is stated that it is sufficient for the phase thickness to satisfy $L_o < \Delta z < k\rho_c^2$, where ρ_c is the correlation radius of the field. From ([1], Eq. (64), Section 6.4.1), we have $\rho_c = (1.46 C_n^2 k^2 \Delta z)^{-3/5}$, so we get the criterium

$$\Delta z < k^{-7/11} (C_n^2)^{-6/11} (1.46)^{-6/11} = 0.81 k^{-7/11} (C_n^2)^{-6/11}. \tag{25}$$

These criteria are the same from the point of view of configuration parameters, albeit with a rather large difference in the multiplying constant, thus leaving the question partly open as to how to choose the discretization.

D. Kolmogorov Phase Screens

Here we specialize the discussion of the trade-off (H1)–(H2), for the Kolmogorov model of turbulence. To compare with the formulas in [1], we note that in ([1], Section 3.3.1), the power spectrum Φ_n of the fluctuations $\tilde{\mu}$ of the index of refraction is

$$\Phi_n(\boldsymbol{\kappa}) = 0.033 C_n^2 |\boldsymbol{\kappa}|^{-11/3} \mathbf{1}_{(L_o^{-1}, l_o^{-1})}(|\boldsymbol{\kappa}|). \tag{26}$$

Since our process μ models the fluctuations of the squared index of refraction, we have $\mu \approx 2\tilde{\mu}$. We also have a different convention of the Fourier transform, which can be reconciled by dividing the formulas in [1] by $(2\pi)^3$. Then, we obtain from definition (3) that our power spectrum $\mathbb{S}$ corresponds to (26) at $\alpha = 5/3$ and $d = 2$, for the normalization constant

$$\chi_{5/3} = 4(2\pi)^3 0.033 C_n^2. \tag{27}$$

We next discuss some configurations motivated by applications and study whether the split-step Fourier method with an independent phase screen approach can be applied according to the above heuristics. For this purpose, we use the Rytov formula (23) for the variance of the intensity.

- **Strong atmospheric turbulence** [1]: if $C_n^2 = 10^{-13}\ \mathrm{m}^{-2/3}$, $l_o = 5/(2\pi)\ \mathrm{mm} \simeq 0.8\ \mathrm{mm}$, $L_o = 10/(2\pi)\mathrm{m} \simeq 1.6\ \mathrm{m}$, $\lambda_o = 1\ \mu\mathrm{m}$, and $Z = 100\ \mathrm{m}$, then the Rytov intensity variance over the whole range interval is $\sigma_R^2(Z) \simeq 0.17^2$, which is too large. To reduce it, we need to discretize the range in steps Δz. If we choose $\Delta z = 10\ \mathrm{m}$, the Rytov intensity variance reduces to $\sigma_R^2(\Delta z) \simeq 0.02^2$, i.e., we have a relative amplitude modulation of 2%, which is acceptable. Furthermore, we can use independent phase screens, because $\Delta z / L_o = 6.25$.
- **Jet plume** [25]: if $C_n^2 = 10^{-9}\ \mathrm{m}^{-2/3}$, $l_o = 1/(2\pi)\ \mathrm{mm} \simeq 0.16\ \mathrm{mm}$, $L_o = 0.5/(2\pi)\ \mathrm{m} = 0.08\ \mathrm{m}$, $\lambda_o = 1.5\ \mu\mathrm{m}$, and $Z = 10\ \mathrm{m}$ [25], then the Rytov intensity variance over the whole range interval is $\sigma_R^2(Z) \simeq 2.1^2$. This gives an unacceptably large relative amplitude modulation of more than 200%. To reduce this modulation to less than 5% [recall criterium (H2)], we need phase screens of thickness $\Delta z < 0.17\ \mathrm{m}$. But then $\Delta z / L_o < 2.12$ and the Markov approximation cannot be applied. Therefore, we need to use correlated phase screens.
- **Aero-optics:** in these applications, lasers mounted on fast-flying aircraft are affected by strong turbulent boundary layers around them [29–31]. The values of specific parameters depend strongly on the specific context, and factors such as the shape of the aircraft play a role. We illustrate a case of extreme turbulence that arises for a relatively short propagation distance $Z = 10\ \mathrm{m}$ and a larger outer scale $L_o = 1\ \mathrm{m}$, by taking $C_n^2 \simeq 10^{-11}\ \mathrm{m}^{-2/3}$ and $\lambda_o = 1\ \mu\mathrm{m}$. Then, according to the criterium (24), we would need $\Delta z < 1.6\ \mathrm{m}$, which means that the phase screens will be correlated.

3. SCE-DFT APPROACH TO GENERATING CORRELATED PHASE SCREENS

We describe here how we sample realizations of the Gaussian random process $U_j(\boldsymbol{x})$, with correlation structure given in Eq. (16). As stated in Section 2.B, this process is isotropic and stationary in both the cross-range $\boldsymbol{x}$ and the range index $j \in \mathbb{Z}$.

We use a smooth embedding extension of the method introduced in [36]. The core idea is to artificially periodize the covariance matrix by embedding it in a larger circulant matrix that can be diagonalized efficiently using the FFT. As long as the embedding matrix is non-negative definite, we can compute its square-root and generate a Gaussian process with the periodized covariance. A suitable subfield of this process gives the desired phase screens.

It is known that the embedding matrix can be made non-negative definite by choosing a large enough embedding [47,39]. Minimal embeddings give non-negative matrices only in special cases [36], so, in practice, it is important to know how to find a suitable embedding. One step in doing so is to introduce smoothing in the embedding process. This eliminates abrupt changes at the boundary of the periodization, which are a cause of undesirable, negative eigenvalues. We refer the interested reader to the studies [48,49,50] that consider various types of smoothing. There exist theoretical bounds on the size of the embedding that guarantee non-negative definiteness, in the presence of smoothing [48,39]. Depending on the type of covariance, these bounds may depend on the mesh size and from the practical point of view, they may suggest larger than needed embeddings for an acceptable approximation of the statistics of the phase screens. There is also a convex optimization approach to finding an optimal circulant embedding [51] that naturally brings some extra computational burden.

Here, we use a different and simple smoothing extension of the circulant embedding method and show that even for embeddings that are much smaller than stated in the theoretical bounds, the negative part of the spectrum of the embedding matrix is very small. This allows the quantification and control of the error of the generated phase screens.

A. Circulant Embedding in One Dimension

To simplify the presentation of our SCE-DFT approach, we begin with the one-dimensional case. Then, in Section 3.B, we describe the extension to higher dimensions, as needed for the generation of the phase screens.

Suppose that we wish to sample a mean zero, stationary Gaussian field $y(x)$, with covariance $\mathscr{C}(x) = \mathbb{E}[y(x')y(x'+x)]$, on a uniform grid $x_j = j/\Delta x$ in the interval $x \in (0, L)$. We count the grid points with $j = 0, \dots, n$, and let $x_n = L$, so that the grid step is $\Delta x = L/n$. The goal is to generate (sample) the Gaussian random column vectors

$$\mathbf{Y} = (y(x_0), \dots, y(x_n))^T, \tag{28}$$

with mean zero and $(n+1) \times (n+1)$ covariance matrix

$$\mathscr{C} = \mathbb{E}\left[\mathbf{Y}\mathbf{Y}^T\right] = (\mathscr{C}(|j-k|\Delta x))_{0 \le j,k \le n}. \tag{29}$$

Note that $\mathscr{C}$ is a non-negative definite and symmetric Toeplitz matrix that is completely characterized by its first row.

The periodization of the covariance is

$$\check{\mathscr{C}}(x) = \begin{cases} \mathscr{C}(x) & \text{for } 0 \le x \le L, \\ \mathscr{C}\,(2L(1+f)-x) & \text{for } L(1+2f) \le x \le 2L(1+f), \end{cases} \tag{30}$$

where $f \ge 0$ is called the embedding fraction. Definition (30) ensures that $\check{\mathscr{C}}(x)$ satisfies periodic boundary conditions at the ends of the interval $[0, 2L(1+f)]$:

$$\check{\mathscr{C}}(x=0) = \check{\mathscr{C}}(x = 2L(1+f)) = \mathscr{C}(0),$$

and thus it can be extended periodically to the whole real line. The choice $f = 0$ gives the minimal embedding, but with the exception of very special cases [36], it is unlikely to give a non-negative covariance. Thus, we take $f > 0$ and note that there is a gap $(L, L(1+2f))$, where $\check{\mathscr{C}}(x)$ remains to be defined.

Assume for simplicity that $N = 2L(1+f)/\Delta x$ is a natural number and define the matrix $\check{\mathscr{C}} = (\check{\mathscr{C}}(|j-k|\Delta x))_{0 \le j,k \le N}$. There are mathematical results [48,47,39] that estimate how large f should be in order to have $\check{\mathscr{C}}$ positive definite. This makes it possible to build an exact and fast sampling scheme, i.e., generate $\mathbf{Y}$ with the correct covariance (29) by generating first a realization $\check{\boldsymbol{y}}$ of the $N+1$-dimensional Gaussian random vector $\check{\boldsymbol{Y}}$ with the covariance $\check{\mathscr{C}}$ by a spectral (FFT) method and then extracting $\boldsymbol{y} = (\check{y}(x_j))_{j=0}^n$. The vector $\boldsymbol{y}$ is then a realization of the $n+1$-dimensional Gaussian random vector $\boldsymbol{Y}$ with the covariance $\mathscr{C}$ since $\mathscr{C} = (\check{\mathscr{C}}(|j-k|\Delta x))_{0 \le j,k \le n}$. This strategy depends on how $\check{\mathscr{C}}(x)$ is defined at $x \in (L, L(1+2f))$. If it is simply set to zero, the jump discontinuities at $x = L$ and $x = L(1+2f)$ induce a significant negative part of the spectrum of the periodized covariance, unless f is very large. The estimates in [39,48] show that this large f depends on the sample grid and diverges to infinity as the grid is refined. However, when the covariance is extended smoothly to the interval $(L, L(1+2f))$, the embedding becomes efficient, with grid-independent embedding fraction f. This is shown in [39,48] for an extension that is differentiable at all orders. Here, we show that we can get guaranteed good results with a small embedding fraction, using a smooth embedding defined by the quadratic polynomial:

$$\check{\mathscr{C}}(x) = \mathscr{C}(L) + \frac{\mathscr{C}'(L)}{2Lf}(x-L)[L(1+2f)-x], \quad \text{for } x \in (L, L(1+2f)). \tag{31}$$

This choice makes $\check{\mathscr{C}}(x)$ symmetric about $x = L(1+f)$ and continuously differentiable. Indeed, we verify from (30) and (31) that $\check{\mathscr{C}}'(L(1+f)) = 0$ and that $\check{\mathscr{C}}(L) = \mathscr{C}(L) = \check{\mathscr{C}}(L(1+2f))$ and $\check{\mathscr{C}}'(L) = \mathscr{C}'(L) = -\check{\mathscr{C}}'(L(1+2f))$. The smoothness of our embedding is essential to ensure that a small embedding fraction f is sufficient to get a nearly exact sampling method with a theoretically derived upper bound on the error of the approximated covariance.

We can always choose f so that $N = 2L(1+f)/\Delta x$ is a natural number. The grid-sampled periodized covariance defines the circulant $N \times N$ Toeplitz matrix $\check{\mathscr{C}}$ with first row:

$$\check{\mathbf{c}} = \left(\check{\mathscr{C}}(j\Delta x)\right)_{0 \le j \le N-1}. \tag{32}$$

The matrix $\check{\mathscr{C}}$ is diagonalized by applying the discrete Fourier transform to the vector $\check{\mathbf{c}}$, and we store its eigenvalues in the vector

$$\mathbf{S} = \mathrm{FFT}(\check{\mathbf{c}}), \tag{33}$$

computed via the FFT. If we divide the eigenvalues into the non-negative and negative ones

$$\mathbf{S}^{(+)} = \left\{\mathbf{S}(j)\mathbb{1}_{\{\mathbf{S}(j)>0\}}\right\}_{j=0}^{N-1}, \qquad \mathbf{S}^{(-)} = \mathbf{S} - \mathbf{S}^{(+)}, \tag{34}$$

we expect that a good embedding corresponds to a small norm of $\mathbf{S}^{-}$.

To generate an approximation of (28), we define the N-dimensional random vector:

$$\check{\mathbf{Y}} = \mathrm{iFFT}\left(\sqrt{\mathbf{S}^{(+)}} .* (\boldsymbol{\eta}^{(1)} + \mathrm{i}\boldsymbol{\eta}^{(2)})\right), \tag{35}$$

where "iFFT" denotes the inverse FFT. Here, the square-root acts term-wise, the operation ".*" represents term-wise multiplication, and $\boldsymbol{\eta}^{(j)}$, $j = 1, 2$ are independent standard Gaussian random vectors. The desired $n+1$-dimensional column vector (28) is approximated by

$$y(x_j) \approx \mathbf{Y}(j) = \mathrm{real}\left[\check{\mathbf{Y}}(j)\right], \qquad j = 0, \dots, n. \tag{36}$$

Note that the vectors $(\check{\mathbf{Y}}(j+k))_{0 \le j \le n}$ have the same distribution for all $k \in \{0, \dots, N-n-1\}$ as a consequence of the periodization, so we could have taken any of these vectors to define $(y(x_j))_{0 \le j \le n}$. Note also that we could have taken the imaginary part in Eq. (36). Therefore, the scheme allows the generation of two or more (correlated) random samples of $\mathbf{Y}$, at once.

In Appendix B, we derive the following result:

$$\left\|\mathbb{E}\left[\mathbf{Y}\mathbf{Y}^T\right] - \mathscr{C}\right\|_2 \le 2\|\mathbf{S}^{(-)}\|_2. \tag{37}$$

It quantifies the error of the approximation of the covariance matrix (29) in terms of the norm of the vector $\mathbf{S}^{-}$ of negative eigenvalues of the embedding matrix. In Section 3.C, we how for three-dimensional simulations, that this norm is negligible even for small embedding fractions f. Therefore, the sampling scheme generates efficiently random phase screens with covariance that is very close to $\mathscr{C}$ and has user controlled error determined by $\|\mathbf{S}^{-}\|$, which is in turn controlled by the embedding fraction f.

B. Circulant Embedding in Higher Dimensions

Here we briefly describe the two- and three-dimensional versions of the SCE-DFT method. The procedure follows [36] and uses the smoothing described above.

Suppose that we wish to sample a two-dimensional, mean zero, stationary Gaussian field $y(\boldsymbol{x})$, for $\boldsymbol{x} = (x_1, x_2) \in (0, L_1) \times (0, L_2)$. We discretize the domain uniformly, on a grid with step sizes $\Delta x_1 = L_1/n_1$ and $\Delta x_2 = L_2/n_2$ and order the grid points left to right, i.e.,

$$(0, 0), (\Delta x_1, 0), \ldots, (n_1 \Delta x_1, 0), (0, \Delta x_2),$$

$$(\Delta x_1, \Delta x_2), \ldots, (n_1 \Delta x_1, \Delta x_2), (0, 2\Delta x_2), \ldots$$

The number of grid points is $n = (n_1 + 1)(n_2 + 1)$ and the $n \times n$ covariance matrix $\mathscr{C}$ of the vector $\mathbf{Y}$ defined by $y(\boldsymbol{x})$ evaluated on the grid is symmetric and block Toeplitz, with $(n_1 + 1) \times (n_1 + 1)$ sized blocks corresponding to a fixed $x_2 = j\Delta x_2$, for $j = 0, \ldots, n_2$. The blocks themselves are also Toeplitz and we denote them by $\mathscr{C}_j$.

The first step is to embed each block $\mathscr{C}_j$ in a square, circulant matrix $\check{\mathscr{C}}_j$ of size $N_1 \times N_1$, where $N_1 > n_1$. This is done as described in Section 3.A. We obtain the $N_1(n_2 + 1) \times N_1(n_2 + 1)$ block Toeplitz matrix

$$\begin{pmatrix} \check{\mathscr{C}}_0 & \check{\mathscr{C}}_1 & \check{\mathscr{C}}_2 & \ldots & \check{\mathscr{C}}_{n_2} \\ \check{\mathscr{C}}_1^T & \check{\mathscr{C}}_0 & \check{\mathscr{C}}_1 & \ldots & \check{\mathscr{C}}_{n_2-1} \\ \check{\mathscr{C}}_2^T & \check{\mathscr{C}}_1^T & \check{\mathscr{C}}_0 & \check{\mathscr{C}}_1 & \ldots \\ & & & \ddots & \\ \check{\mathscr{C}}_{n_2}^T & \check{\mathscr{C}}_{n_2-1}^T & \check{\mathscr{C}}_{n_2-2}^T & \ldots & \check{\mathscr{C}}_0 \end{pmatrix} \tag{38}$$

that is then cyclically embedded in an $N_1 N_2 \times N_1 N_2$ block circulant matrix $\check{\mathscr{C}}$ with circulant blocks. The matrix $\check{\mathscr{C}}$ is diagonalized using the two-dimensional FFT applied to $\check{\mathbf{c}} = (\check{\mathscr{C}}(j_1 \Delta x_1, j_2 \Delta x_2))_{0 \le j_1 \le N_1 - 1, 0 \le j_2 \le N_2 - 1}$.

Note that we do not need to store the $N_1 N_2 \times N_1 N_2$ matrix $\check{\mathscr{C}}$. Due to the block circulant structure, we only need the $N_1 \times N_2$ matrix $\check{\mathbf{c}}$. The generation of the Gaussian random vector is obtained as in Section 3.A. The computational cost is $O(M \log M)$ flops, and the storage requirement is $O(M)$, for $M = N_1 N_2$.

Similarly, consider a three-dimensional, mean zero, stationary random field $y(\boldsymbol{x})$, evaluated at $\boldsymbol{x} = (x_1, x_2, x_3)$ in a uniform grid that discretizes a rectangular domain $(0, L_1) \times (0, L_2) \times (0, L_3)$. The covariance $\mathscr{C}$ is block symmetric and block Toeplitz matrix, whose blocks correspond to a fixed x_3. Each such block has the properties of the two-dimensional covariance considered above. The relations (32), (33), and (35) in the one-dimensional case generalize to three dimensions in the following way: the step in (32) is generalized by forming a third-order tensor via smooth embedding in three dimensions. The embedding fractions can be different in different directions. In our simulations, we use an embedding fraction $f_x = 0.5$ in the lateral directions and $f_z = 0.25$ in the range direction. This gives a modest increase in the computational cost and storage requirement. The generalization of step (33) uses the three-dimensional FFT applied to $\check{\mathbf{c}} = (\check{\mathscr{C}}(j_1 \Delta x_1,\ \ j_2 \Delta x_2,\ \ j_3 \Delta x_3))_{0 \le j_1 \le N_1 - 1,\, 0 \le j_2 \le N_2 - 1,\, 0 \le j_3 \le N_3 - 1}$ that produces a tensor of size $N_1 \times N_2 \times N_3$ comprising the eigenvalues. Step (35) is generalized by replacing the one-dimensional iFFT with a three-dimensional iFFT and by replacing the $\boldsymbol{\eta}^{(j)}$, $j = 1, 2$ with third-order tensors with independent Gaussian entries. The simulated field is then generated by taking the real (or imaginary) part of a sub-tensor of size $n_1 \times n_2 \times n_3$. The computational cost is $O(M \log M)$ flops, and the storage requirement is $O(M)$, for $M = N_1 N_2 N_3$.

C. Generation of the Phase Screens

The phase screens are generated with the three-dimensional SCE-DFT method described above, for the covariance given in Eq. (16). We illustrate the results for the Kolmogorov spectrum, i.e., $\alpha = 5/3$. The inner scale is $l_o = 8$ mm and the outer scale is $L_o = 1$ m. The screens are generated on a cross-range square domain of side $L_x = 0.4$ m and the distance of propagation is $Z = 1.3$ m. There are $n_1 = n_2 = 2^{11}$ grid points in the cross-range directions and $n_z = 6$ phase screens. Here and below we denote by the bold letter $\boldsymbol{x} = (x_1, x_2)$ the vector of lateral coordinates and by z the range coordinate. Note also that x is used below for either x_1 or x_2.

Figure 1 shows the *spectral accuracy* parameter

$$\mathcal{E} := \|\mathbf{S}^{(-)}\|_2 / \|\mathbf{S}\|_2 \tag{39}$$

as a function of the cross-range embedding fraction f_x and with the embedding fraction in range fixed at $f_z = 0.25$. We see that even with a small f_x, the parameter $\mathcal{E}$ is of the order of 2%. Moreover, the plot has an "L" curve type behavior and indicates an optimal $f_x \approx 0.65$, where $\mathcal{E} \approx 0.2\%$. We use $f_x = 0.5$ and $f_z = 0.25$, henceforth.

The choice of the smooth embedding we made in (31) affects the spectral accuracy, as shown in Fig. 1. The minimum noted in Fig. 1 corresponds to the particular choice of f that makes $\check{\mathscr{C}}$ twice continuously differentiable. We discuss the qualitative

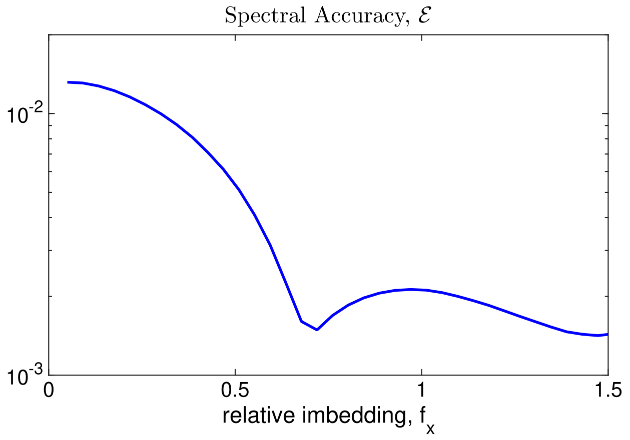

Fig. 1. Spectral accuracy $\mathcal{E}$ as a function of the cross-range embedding fraction, f_x.

behavior of the spectral accuracy and the relation to the smooth embedding method in more detail in C.

The left plot in Fig. 2 shows the empirical phase screen correlations with the blue dashed curve and the specified correlations $\boldsymbol{x} \mapsto \mathbb{E}[\mathbf{Y}(\boldsymbol{x}' + \boldsymbol{x}, j_z)\mathbf{Y}(\boldsymbol{x}', j_z)]/\mathbb{E}[\mathbf{Y}^2(\boldsymbol{x}', j_z)]$ deriving from (16) with the red solid curve. Here again, we use $n_z = 6$. With the smooth embedding, the correlation of the sampled field $\mathbf{Y}$ is close to the target correlation. The right plot shows the evolution in $m\Delta z$ of the (normalized) variance of the cumulative medium fluctuations in range

$$\mathcal{Y}(m) := \mathbb{E}\left[\left(\sum_{j_z=1}^{m}\mathbf{Y}(\boldsymbol{x}, j_z)\right)^2\right] / \mathbb{E}\left[\left(\sum_{j_z=1}^{n_z}\mathbf{Y}(\boldsymbol{x}, j_z)\right)^2\right],$$

for $\boldsymbol{x} = (x_1, x_2)$, $m \in \{0, \ldots, n_z\}$.

4. PARAXIAL PROPAGATION WITH DEPENDENT AND INDEPENDENT PHASE SCREENS

In this section, we present numerical simulations of the paraxial wave equation using both independent and correlated phase screens. In light of the discussion in Sections 2.C and 2.D, one may wonder what happens when using independent phase screens of thickness Δz that violate (H1) or a criterion of type (H2) or both? The answer depends on the output quantity of interest. We show here that the errors are seen mostly in the estimates of the high-order moments, which are more sensitive to the tail of the distribution of the wave field. This is important since, in the optical context, one is often interested in the fourth-order moments that characterize the statistics of speckle. We remark that the conditions (24) and (25) differ by a factor of 25. Although they indicate a specific parametric condition for phase screen discretization, they do not give a very precise condition for the choice of the discretization step.

We use the Strang splitting method summarized in Eq. (14). The correlated phase screens are generated as described in Section 3, with the covariance given by (16). The smooth embedding fractions are $f_z = 0.25$ in the z-direction (index of the screen) and $f_x = 0.5$ in the two cross-range directions. For the simulations with independent phase screens, the transverse covariance is given by Eq. (16) with $j = 0$, rather than the approximation (22), which holds only when $\Delta z \gg L_o$. We show results with $d = 2$, i.e., propagation in three dimensions.

We choose the length scales relative to the outer scale L_o as follows: the wavelength is $\lambda_o/L_o = 2 \times 10^{-6}$, the inner scale is $l_o/L_o = 8 \times 10^{-3}$, and the total propagation distance is $Z/L_o = 1.3$. The initial profile $\psi_0(\boldsymbol{x})$ is a Gaussian centered at the origin and with standard deviation $r_o/L_o = 2 \times 10^{-2}$ (scaled to have unit maximum amplitude). The simulation domain is the cuboid with a square cross-section of side $L_x/L_o = 0.4$. This is discretized with 2^{11} grid points in each lateral direction. Thus, in particular, if the outer scale is $L_o = 1m$ then the wavelength is 2 μm. We moreover consider both the cases with correlated screens (left plots) and independent screens (right plots). The plots show empirical estimates based on 300 independent simulations.

The spectral exponent is $\alpha = 5/3$, corresponding to Kolmogorov turbulence. We choose the Kolmogorov model because of its popularity in the optics literature, but other, non-Kolmogorov models [52] may be used as well. We consider strong turbulence corresponding to $C_n^2 L_o^{2/3} = 2 \times 10^{-9}$ and $C_n^2 L_o^{2/3} = 6 \times 10^{-10}$, respectively.

In Fig. 3, we show the estimated mean intensity

$$I_X(|\boldsymbol{x}|) = \mathbb{E}\left[|\psi(\boldsymbol{x}, Z)|^2\right]. \tag{40}$$

In the empirical (Monte Carlo) estimation, we exploit the radial symmetry of the source and the statistical isotropy in cross-range and average over the direction in the cross-range plane. Here and below, the green, green dashed, red, red dashed, blue, and blue dashed lines correspond to numerical simulations using 1, 2, 4, 6, 14, and 22 phase screens, respectively. We see that even in extreme turbulence, the intensity profile is not much affected by the propagation, and it is not sensitive to the phase screen discretization. The intensity profile is captured well, also with independent phase screens.

In Fig. 4, we show the estimated field covariance

$$C_X^{(1)}(|\boldsymbol{x}|) = \mathrm{real}\left\{\mathbb{E}\left[\psi(\mathbf{0}, Z)\overline{\psi(\boldsymbol{x}, Z)}\right] - \mathbb{E}\left[\psi(\mathbf{0}, Z)\right]\mathbb{E}\left[\overline{\psi(\boldsymbol{x}, Z)}\right]\right\}. \tag{41}$$

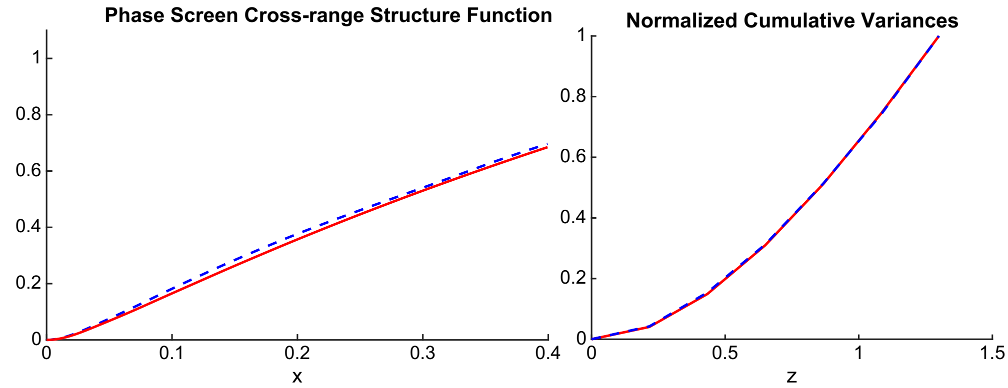

Fig. 2. Blue dashed line in the left plot is the empirical phase screen structure function in cross-range, with the range offset being zero, while the red line is the specified structure function. Due to the isotropy in cross-range, the abscissa in the left plot is $x = |\boldsymbol{x}|$. The right plot is analogous but shows the normalized variances of the cumulative fluctuations in range $z = m\Delta z$, $m \in \{0, \ldots, n_z\}$. For both plots, the abscissa is in units of L_o. The estimates are based on 300 realizations.

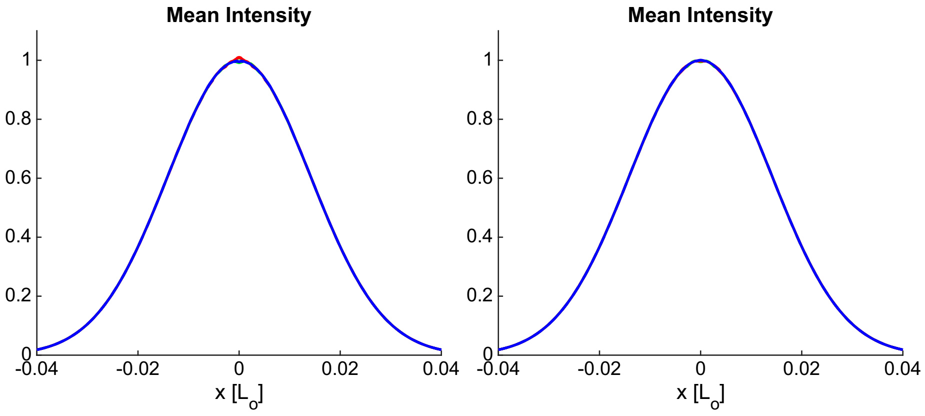

Fig. 3. Intensity profile is insensitive to the discretization. The left plot corresponds to correlated screens and the right plot to independent screens. Here, $C_n^2 L_o^{2/3} = 2 \times 10^{-9}$ and the abscissa is $x = |\boldsymbol{x}|$ in units of L_o. Henceforth, the green, green dotted, red, red dotted, blue, and blue dotted lines correspond to 1, 2, 4, 6, 14, and 22 phase screens, respectively. The curves are difficult to distinguish because of the agreement.

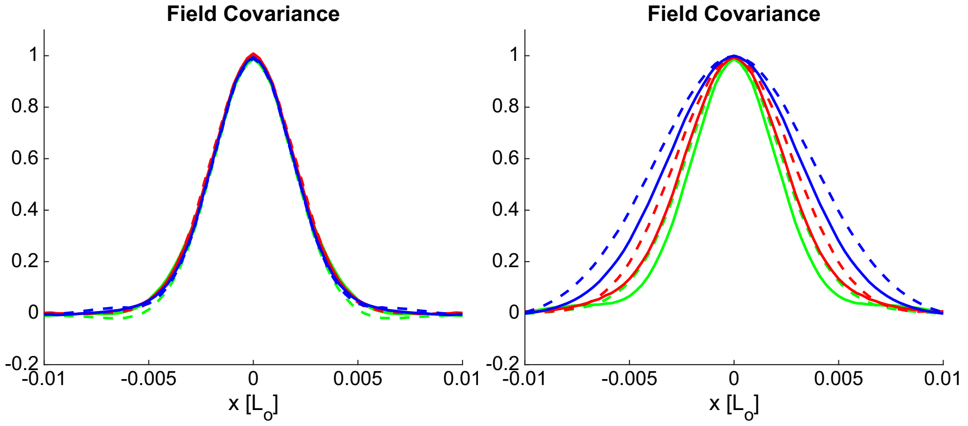

Fig. 4. Field covariance is insensitive to the discretization when using correlated screens (left plot). It depends strongly on the phase screen discretization for independent phase screens (right plot). Here $C_n^2 L_o^{2/3} = 2 \times 10^{-9}$ and the abscissa is $x = |\boldsymbol{x}|$ in units of L_o.

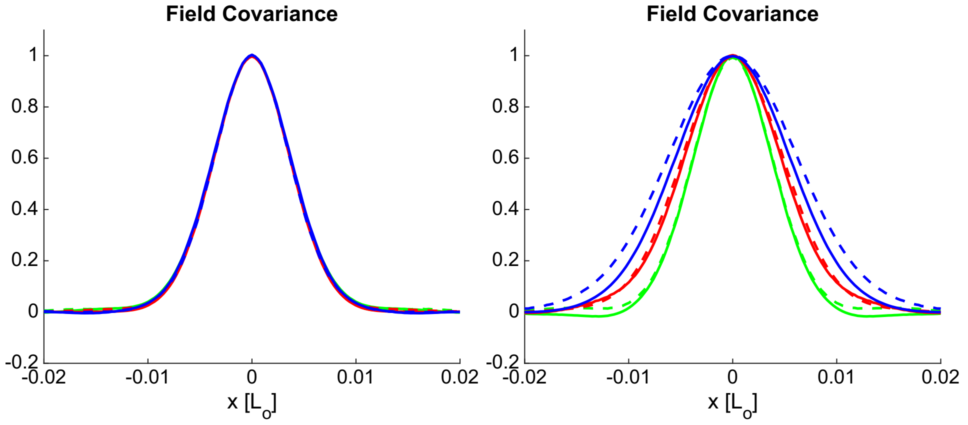

Fig. 5. This is analogous to Fig. 4, but the medium fluctuations are weaker, with $C_n^2 L_o^{2/3} = 6 \times 10^{-10}$. Observe that the covariance has a wider support.

We observe that the covariance, which depends on the phase of the wave field, is rather insensitive to the number of phase screens as long as they are correlated. It is approximated well even by one phase screen. However, the independent phase screen approach for more than one phase screen does not give an accurate answer, because the condition (H1) is violated. Figure 5 corresponds to Fig. 4 just with $C_n^2 L_o^{2/3} = 6 \times 10^{-10}$ rather than $C_n^2 L_o^{2/3} = 2 \times 10^{-9}$. We observe that the support of the field covariance depends on the strength of the turbulence, i.e., it is tighter in Fig. 4 than in Fig. 5.

In Fig. 6, we plot the standard deviation of the intensity

$$S_X(|\boldsymbol{x}|) = \left\{ \mathbb{E}\left[|\psi(\boldsymbol{x}, Z)|^4 \right] - (I_X(|\boldsymbol{x}|))^2 \right\}^{1/2} \tag{42}$$

as a function of $|\boldsymbol{x}|$, where I_X is defined in (40). This defines the scintillation index $\sigma_I^2 = S_X^2(|\boldsymbol{x}|)/I_X^2(|\boldsymbol{x}|)$. We observe from the right plot that the intensity variance is not captured well using the independent phase screen approach. Figure 7 is analogous to Fig. 6, just with $C_n^2 L_o^{2/3} = 6 \times 10^{-10}$ instead of $C_n^2 L_o^{2/3} = 2 \times 10^{-9}$.

Figure 8 shows the intensity standard deviation at its maximum, which is at the center of the beam, i.e., at zero-cross-range

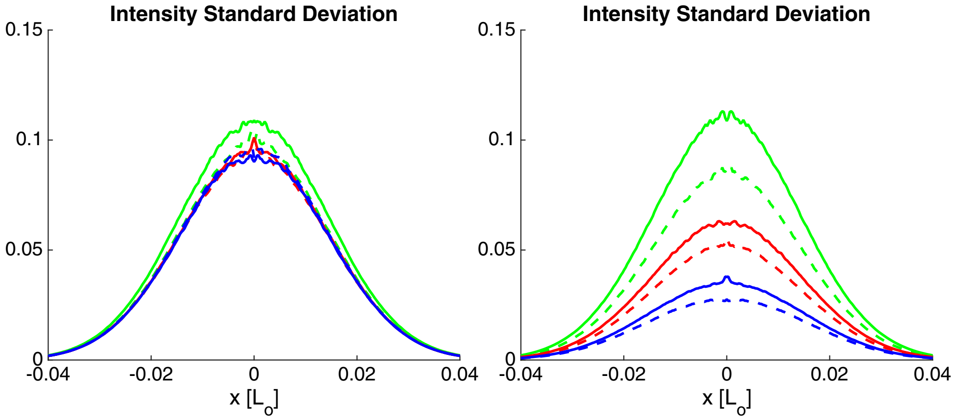

Fig. 6. Intensity standard deviation $S_X(\mathrm{x})$, where $\mathrm{x} = |\boldsymbol{x}|$, for $C_n^2 L_o^{2/3} = 2 \times 10^{-9}$. The left plot corresponds to correlated screens and the right plot to independent screens. Observe the dependence of $S_X(\mathrm{x})$ on the discretization, i.e., the number of phase screens. We observe convergence only when using correlated screens. Since in the Monte Carlo averaging we exploit the radial symmetry of the source and average over radial direction in the $\boldsymbol{x}$ plane, the sample variability is a bit larger at $\boldsymbol{x} = \mathbf{0}$.

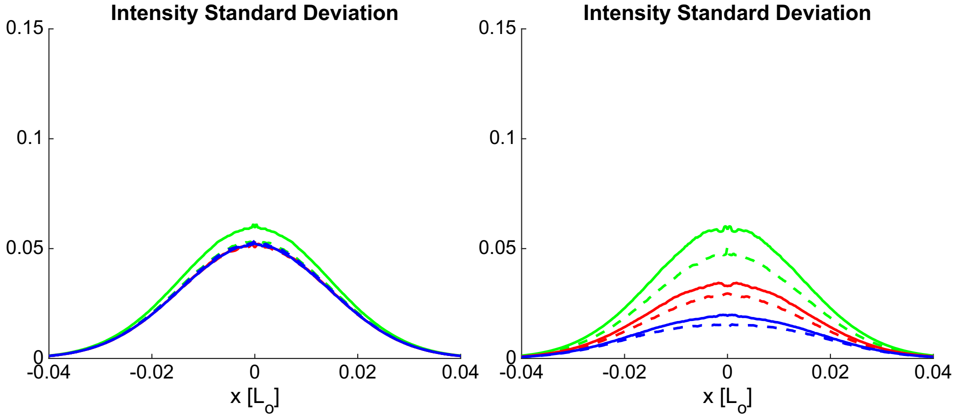

Fig. 7. This is analogous to Fig. 6, but the medium fluctuations are weaker, with $C_n^2 L_o^{2/3} = 6 \times 10^{-10}$.

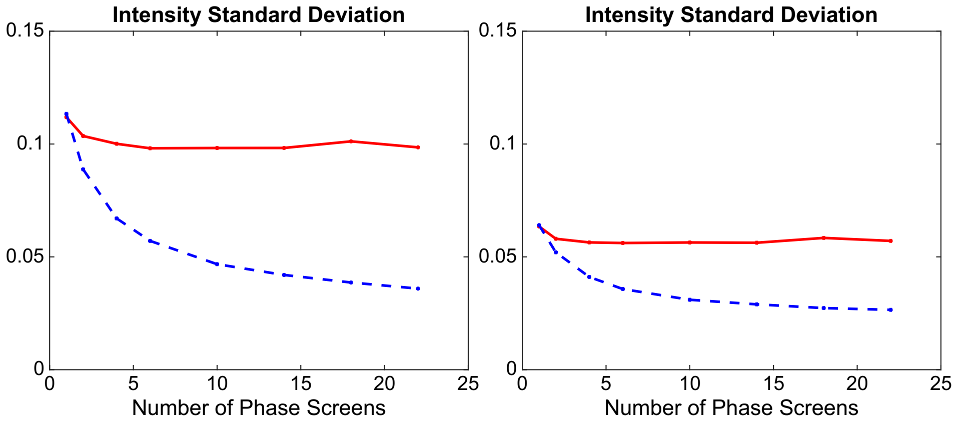

Fig. 8. Figure shows the standard deviation of the intensity at the beam center as a function of the number of phase screens. The left plot is for $C_n^2 L_o^{2/3} = 2 \times 10^{-9}$ and the right plot for $C_n^2 L_o^{2/3} = 6 \times 10^{-10}$. The red solid line corresponds to correlated screens and the blue dashed line to independent phase screens. Again, we observe convergence when using correlated phase screens, but not when using independent ones.

offset, for $C_n^2 L_o^{2/3} = 2 \times 10^{-9}$ and $C_n^2 L_o^{2/3} = 6 \times 10^{-10}$, respectively. The red solid line corresponds to correlated screens and the blue dashed line to independent phase screens. While the intensity standard deviation (scintillation) quickly converges with correlated phase screens, no discretization Δz captures this quantity well when using independent phase screens. Indeed, the intensity standard deviation depends on the fourth moment of the wave field and is more sensitive to the distribution tail of the wave field as compared to low-order moments, and the simulations show that capturing well this tail requires correlated phase screens.

Note that the independent phase screen approach with many independent phase screen, underestimates the intensity standard deviation. This is because using many independent phase screens means that the integral in the range of the medium fluctuations has a variance that is too small. Note also that the wave statistics are non-Gaussian, since the intensity variance function is far from the square modulus of the field variance function.

From Fig. 8, we can observe that the condition on the number of phase screens to use in order to capture the scintillation with high accuracy is similar for the two levels of medium fluctuations considered, albeit the convergence appears a bit faster in the case with weak medium fluctuation, conforming with the condition in (24) with the number of required phase screens scaling with turbulence level.

5. CONCLUSION

In typical regimes of propagation through turbulence, the use of independent phase screens in the split-step Fourier method for wave propagation is well justified. However, there are regimes of extreme turbulence where correlated phase screens are needed. We considered such regimes arising in laser beam propagation through very strong turbulence. The results extend to general models of turbulence and are relevant for propagation through atmospheric turbulence or through oceanic or turbulent water layers [53,54].

We reviewed, for the case of Kolmogorov turbulence, the validity of using independent phase screens and motivated the use of correlated screens for propagation through extreme turbulence. We showed that classic criteria for phase screen discretization may not be useful to achieve high accuracy for speckle statistics, in particular in the regime of small scintillation. We showed moreover that while second-order wave field moments may be well approximated with a coarse phase screen discretization with independent phase screens, to resolve well scintillation and speckle statistics, one would need a finer discretization. Furthermore, we presented a smooth circulant embedding algorithm, called SCE-DFT, for sampling efficiently the random correlated phase screens. With this algorithm, we performed three-dimensional Monte Carlo simulations and quantified the artifacts produced by the independent phase screen approach on the statistics of the wave field. Indeed, these artifacts are visible mostly in the estimates of the fourth-order moments of the wave field that characterize the statistics of speckle. We also showed that the split-step Fourier method with correlated phase screens gives stable results with respect to the phase screen thickness.

APPENDIX A: DERIVATION OF THE COVARIANCE OF THE PHASE SCREENS

In this Appendix, we give the derivation of the covariance of the phase screens, stated in Eq. (16) and the approximation for the asymptotic regime $\Delta z \gg L_o > l_o$, as stated in Eq. (21).

- The first line in Eq. (16) is due to stationarity. For the second line, we use

$$\begin{aligned}\mathbb{E}[U_j(\boldsymbol{x})U_0(\mathbf{0})] &= \int_{j\Delta z}^{(j+1)\Delta z} \mathrm{d}z_1 \int_0^{\Delta z} \mathrm{d}z_2\, \mathbb{E}[\mu(\boldsymbol{x}, z_1)\mu(\mathbf{0}, z_2)] \\ &= \int_{j\Delta z}^{(j+1)\Delta z} \mathrm{d}z_1 \int_0^{\Delta z} \mathrm{d}z_2\, R_d(|(\boldsymbol{x}, z_1 - z_2)|) \\ &= \int_{(j-1)\Delta z}^{(j+1)\Delta z} \mathrm{d}s\ \ (\Delta z - |s - j\Delta z|)\, R_d(|(\boldsymbol{x}, s)|),\end{aligned}$$

which gives the desired result.

- Denoting $j_1(u) = J_0(u)$ and $j_2(u) = \mathrm{sinc}(u)$, we have

$$\begin{aligned}\mathbb{E}[U_0(\mathbf{0})^2] &= 2\int_0^{\Delta z} \mathrm{d}s\, (\Delta z - s)\, R_d(|(\mathbf{0}, s)|) \\ &= \frac{\chi_\alpha}{\pi^d}\int_0^{\Delta z} \mathrm{d}s \int_{s/L_o}^{s/l_o} \mathrm{d}u\, u^{-\alpha} j_d(u)(\Delta z - s)s^{\alpha-1} \\ &= \frac{\chi_\alpha}{\pi^d}\int_0^{\Delta z/l_o} \mathrm{d}u\, u^{-\alpha} j_d(u) \int_{l_o u}^{L_o u \wedge \Delta z} \mathrm{d}s\, (\Delta z - s)s^{\alpha-1},\end{aligned}$$

which gives (17) after computing the integral in s.

- We have without any approximation for $d = 2$

$$\begin{aligned}\mathbb{E}[U_n(\mathbf{0})U_0(\mathbf{0})] &= \frac{\chi_\alpha \Delta z^2}{2\pi^2\alpha}\int_0^{l_o^{-1}} \left[(\kappa_z \vee L_o^{-1})^{-\alpha} - l_o^\alpha\right] \\ &\quad \times \mathrm{sinc}^2\left(\frac{\kappa_z \Delta z}{2}\right) \cos\,(\kappa_z n \Delta z)\, \mathrm{d}\kappa_z \\ &= \frac{\chi_\alpha \Delta z}{2\pi^2\alpha}\int_0^{\Delta z/l_o} \left[L_o^\alpha((s\,L_o/\Delta z) \vee 1)^{-\alpha} - l_o^\alpha\right] \\ &\quad \times \mathrm{sinc}^2\left(\frac{s}{2}\right) \cos(ns)\mathrm{d}s\,.\end{aligned}$$

If $\Delta z \gg L_o > l_o$, then this can be approximated by

$$\mathbb{E}[U_n(\mathbf{0})U_0(\mathbf{0})] \simeq \frac{\chi_\alpha \Delta z(L_o^\alpha - l_o^\alpha)}{2\pi^2\alpha}\int_0^\infty \mathrm{sinc}^2\left(\frac{s}{2}\right)\cos\,(ns)\, \mathrm{d}s\,,$$

which gives (20) and (21) for $\boldsymbol{x} = \mathbf{0}$ because $\int_0^\infty \mathrm{sinc}^2(\frac{s}{2})\cos(ns)\mathrm{d}s = \pi\,\mathbf{1}_0(n)$. The calculations of the other moments are similar.

APPENDIX B: DERIVATION OF THE ERROR BOUND (37)

Assume for convenience, but without loss of generality, that $k = 0$ in (36). Define the $N \times N$ diagonal matrix $\mathbf{D} = \{\mathbb{1}_{\{j=\ell\}\bigcap\{0\le j\le n\}}\}_{j,\ell=0}^{N-1}$, with first $n+1$ diagonal entries equal to 1 and zero otherwise. This selects the entries of $\mathbf{Y}$, as stated in Eq. (36) for $k = 0$. Recall that the embedding matrix is $\check{\mathscr{C}}$ and that it is diagonalized by the discrete Fourier transform. If we denote by $\mathbf{F}$ the unitary matrix that represents this transform, we have

$$\check{\mathscr{C}}\mathbf{F} = \mathbf{F}\,\mathrm{diag}(\mathbf{S}),$$

with $\mathrm{diag}(\mathbf{S})$ being the diagonal matrix with entries $\mathbf{S}(j)$. Then, using the definition (36) and the splitting (34) of the eigenvalues into the positive and negative parts, we get

$$\begin{aligned}\left\|\mathbb{E}\left[\mathbf{Y}\mathbf{Y}^T\right] - \mathscr{C}\right\|_2 &= \left\|\mathbf{D}\left(\mathrm{real}(\mathbf{F})\mathrm{diag}(\mathbf{S}^{(-)})\mathrm{real}(\mathbf{F})\right.\right.\\ &\qquad \left.\left.+\ \mathrm{imag}(\mathbf{F})\mathrm{diag}(\mathbf{S}^{(-)})\mathrm{imag}(\mathbf{F})\right)\mathbf{D}\right\|_2\\ &\le 2\|\mathbf{S}^{(-)}\|_2.\end{aligned}$$

APPENDIX C: ON THE SPECTRAL ACCURACY

We discuss here aspects of the smooth embedding in the context of the SCE-DFT method for sampling a Gaussian random field. Our smooth embedding corresponds to a second-order spline interpolation, as given in (31). We compare it here with two other smooth embedding methods. For this purpose, it suffices to consider the one-dimensional case and sampling of a centered random field with a Gaussian correlation function.

The three smooth embedding methods are: the second- and fourth-order spline interpolations and smooth tapering to zero. We use a configuration as introduced in Section 3.A. In the parameterization introduced, there we use $n = 2^{11}$ and $L = 0.4$; moreover, the Gaussian correlation function for $\mathscr{C}$ has width $\sigma = 0.3$. The second- and fourth-order smooth embeddings can be written as

$$\check{\mathscr{C}}^{(s2)}(x) = a^{(s2)} + b^{(s2)}h^2(x) \tag{C1}$$

and

$$\check{\mathscr{C}}^{(s4)}(x) = a^{(s4)} + b^{(s4)}h^2(x) + c^{(s4)}h^4(x), \tag{C2}$$

respectively, while the smooth tapering to zero is defined by

$$\check{\mathscr{C}}^{(tz)}(x) = (\mathscr{C}\phi)(x) + (\mathscr{C}\phi)(2(1+f)L - x), \tag{C3}$$

for $x \in (L, (1+2f)L)$. Here we defined

$$h(x) = \frac{x - L(1+f)}{fL}, \tag{C4}$$

$$a^{(s2)} = \mathscr{C}(L) + c_1/2, \quad b^{(s2)} = -c_1/2, \tag{C5}$$

$$\begin{aligned}a^{(s4)} &= \mathscr{C}(L) + (5c_1 + c_2)/8, \quad b^{(s4)} = -(3c_1 + c_2)/4,\\ c^{(s4)} &= (c_1 + c_2)/8,\end{aligned} \tag{C6}$$

with $c_1 = (fL)\mathscr{C}'(L)$, $c_2 = (fL)^2\mathscr{C}''(L)$, and

$$\phi(x) = \frac{\eta((\kappa - |x/L|)/(\kappa - 1))}{\eta((\kappa - |x/L|)/(\kappa - 1)) + \eta((|x/L| - 1)/(\kappa - 1))}, \tag{C7}$$

$$\eta(x) = \begin{cases}\exp(-x^{-1}) & \text{for } x > 0,\\ 0 & \text{for } x \le 0\end{cases}, \tag{C8}$$

for $\kappa = 1 + f/2$. Recall that for $x \in ((0, L)\bigcup((1+2f)L, 2(1+f)L))$, the circulant embedding correlation profile is given by (30).

In Fig. 9, we show the spectral accuracy $\mathcal{E}$ defined by (39) as a function of the embedding fraction. Note first that the spline interpolation that we have introduced has a much better spectral accuracy at small embedding fraction than the classic padding to zero approach. Moreover, the second- and fourth-order spline interpolation accuracy curves cross at the embedding fraction:

$$f^* := -\mathscr{C}'(L)/[L\mathscr{C}''(L)]. \tag{C9}$$

Indeed, for $f = f^*$ the second- and fourth-order spline interpolation schemes coincide because $\check{\mathscr{C}}^{(s2)}$ has a second-order derivative that is continuous as $x = L$. For small embedding fractions $f < f^*$ the second-order spline interpolation is the optimal among the three smooth pasting approaches. Note finally that for all embedding fractions considered, here the fourth-order spline scheme has significantly better accuracy than the padding to zero scheme.

In Fig. 10, we show the correlations profiles $\check{\mathscr{C}}^{(c)}(x)$, $x \in (0, 2(1+f))$ for $f = 1.5$ and $c \in \{s2, s4, tz\}$. Note that the fourth-order scheme has a profile that looks similar in magnitude to the tapering to zero scheme for this embedding fraction. However, the fourth-order scheme gives much better spectral accuracy, as shown in Fig. 9. Note also that for large embedding fractions the second-order scheme gives a correlation profile with large amplitude in the pasting section, which conforms with the corresponding spectral accuracy curve in Fig. 9 that

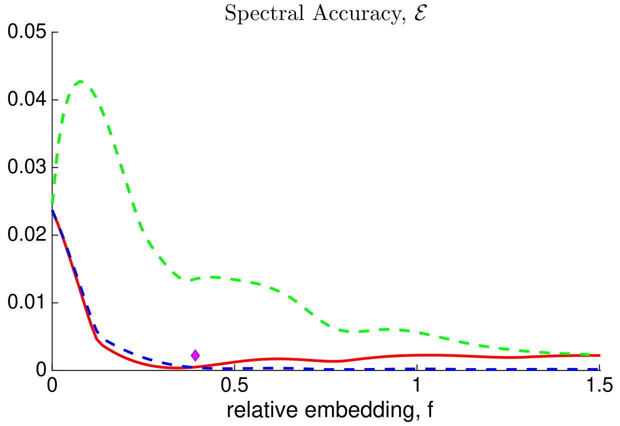

Fig. 9. Spectral accuracy $\mathcal{E}$ as a function of the embedding fraction, f. The solid-red and dashed-blue curves correspond to the second- and fourth-order embedding splines, respectively, while the dashed-green curve is for the tapering to zero embedding of the form (C3) with ϕ defined by (C7). The magenta diamond corresponds to $f = f^*$ defined by (C9), which makes the second-order derivative for the second-order spline continuous at this point so that the second-order spline then coincides with the fourth-order spline. Here $\mathscr{C}$ is a Gaussian correlation function of width $\sigma = 0.3$ and $L = 0.4$.

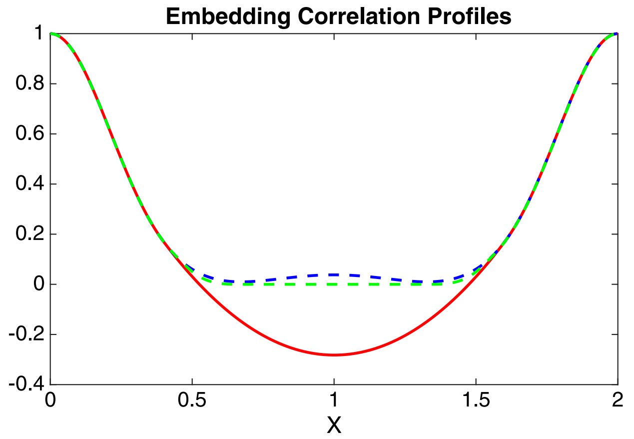

Fig. 10. Correlations profiles used to define the circulant embedding for the embedding fraction $f = 1.5$. The configuration is the same as the one in Fig. 9.

has a minimum around the embedding fraction f^*, where this method is optimal.

The qualitative behavior seen in the above illustration motivates the excellent behavior we have obtained in this paper using the SCE-DFT method based on second-order spline interpolation.

Funding. Office of Naval Research (N000142612023); United States Air Force Office of Scientific Research (FA9550-22-1-0077, FA9550-22-1-0176).

Disclosures. The authors declare no conflicts of interest.

Data availability. Data underlying the results presented in this paper are not publicly available at this time but may be obtained from the authors upon reasonable request.

REFERENCES

1. L. C. Andrews and R. L. Phillips, *Laser Beam Propagation through Random Media* (SPIE-International Society for Optical Engineering, 2005).
2. A. Ishimaru, *Wave Propagation and Scattering in Random Media* (Academic, 1978).
3. V. I. Tatarskii, A. Ishimaru, and V. U. Zavorotny, eds., *Wave Propagation in Random Media (Scintillation)* (SPIE, 1993).
4. G. Bal and A. Nair, "Splitting algorithms for paraxial and Itô-Schrödinger models of wave propagation in random media," arXiv (2025).
5. J.-P. Fouque, G. Papanicolaou, and Y. Samuelides, "Forward and Markov approximation: the strong-intensity-fluctuations regime revisited," Waves Random Media **8**, 303–314 (1998).
6. J. Garnier and K. Sølna, "Coupled paraxial wave equations in random media in the white-noise regime," Ann. Appl. Probab. **19**, 318–346 (2009).
7. D. A. Dawson and G. C. Papanicolaou, "A random wave process," Appl. Math. Optim. **12**, 97–114 (1984).
8. G. Bal and A. Nair, "Complex Gaussianity of long-distance random wave processes," Arch. Ration. Mech. Anal. **249**, 65 (2025).
9. J. Garnier and K. Sølna, "Fourth-moment analysis for wave propagation in the white-noise paraxial regime," Arch. Ration. Mech. Anal. **220**, 37–81 (2016).
10. L. Borcea, J. Garnier, and K. Sølna, "Paraxial wave propagation in random media with long-range correlations," SIAM J. Appl. Math. **83**, 25–51 (2023).
11. R. F. Cahalan and J. B. Snider, "Marine stratocumulus structure," Remote Sens. Environ. **28**, 95–107 (1989).
12. B. L. Madhavan, H. Deneke, J. Witthuhn, *et al.*, "Multiresolution analysis of the spatiotemporal variability in global radiation observed by a dense network of 99 pyranometers," Atmos. Chem. Phys. **17**, 3317–3338 (2017).
13. G. Bal, T. Komorowski, and L. Ryzhik, "Asymptotics of the solutions of the random Schrödinger equation," Arch. Ration. Mech. Anal. **200**, 613–664 (2011).
14. C. Gomez and O. Pinaud, "Fractional white-noise limit and paraxial approximation for waves in random media," Arch. Ration. Mech. Anal. **226**, 1061–1138 (2017).
15. R. J. Adler, *The Geometry of Random Fields* (SIAM, 2010).
16. K. Furutsu and Y. Furuhama, "Spot dancing and relative saturation phenomena of irradiance scintillation of optical beams in a random medium," Optica **20**, 707–719 (1973).
17. J. Garnier and K. Sølna, "Scintillation in the white-noise paraxial regime," Commun. Part. Differ. Equat. **39**, 626–650 (2014).
18. G. Bal and L. Ryzhik, "Time splitting for wave equations in random media," ESAIM Math. Model. Numer. Anal. **38**, 961–987 (2004).
19. W. Bao, J. Shi, and P. A. Markowich, "On time-splitting spectral approximations for the Schrödinger equation in the semiclassical regime," J. Comput. Phys. **175**, 487–524 (2002).
20. M. Charnotskii, "Wave propagation modeling with non-Markov phase screens," J. Opt. Soc. Am. A **33**, 561–569 (2016).
21. M. Spivack and B. J. Uscinski, "The split-step solution in random wave propagation," J. Comput. Appl. Math. **27**, 349–361 (1989).
22. A. Belmonte, "Feasibility study for the simulation of beam propagation: consideration of coherent lidar performance," Appl. Opt. **39**, 5426–5445 (2000).
23. C. Gomez and O. Pinaud, "Asymptotics of a time-splitting scheme for the random Schrödinger equation with long-range correlation," ESAIM Math. Model. Numer. Anal. **48**, 411–431 (2014).
24. N. F. Borisova, I. V. Ivanova, and V. S. Sirazetdinov, "Numerical simulation of laser beam propagation through the turbulent jet from an aero-engine," Atmos. Ocean. Opt. **16**, 795–799 (2003).
25. L. Sjöqvist, "Laser beam propagation in jet engine plume environments: a review," Proc. SPIE **7115**, 71150C (2008).
26. J. L. Barrett and P. A. Budni, "Laser beam propagation through strong turbulence," J. Appl. Phys. **71**, 1124–1127 (1992).
27. C. B. Hogge and W. L. Visinsky, "Laser beam probing of jet exhaust turbulence," Appl. Opt. **10**, 889–892 (1971).
28. V. S. Sirazetdinov, "Experimental study and numerical simulation of laser beams propagation through the turbulent aerojet," Appl. Opt. **47**, 975–985 (2008).
29. E. J. Jumper and E. J. Fitzgerald, "Recent advances in aero-optics," Prog. Aerosp. Sci. **37**, 299–339 (2001).
30. M. kalensky, S. Gordeyev, M. R. Kemnetz, *et al.*, "Aero-optical effects, part I. System-level considerations: tutorial," J. Opt. Soc. Am. A **41**, 2163–2174 (2024).
31. M. kalensky, S. Gordeyev, M. R. Kemnetz, *et al.*, "Aero-optical effects, part II. Sources of aberrations: tutorial," J. Opt. Soc. Am. A **41**, 2175–2187 (2024).
32. N. De Lucca, S. Gordeyev, and E. Jumper, "The airborne aero-optics laboratory, recent data," Proc. SPIE **8395**, 839508 (2012).
33. M. Shinozuka and C. M. Jan, "Digital simulation of random processes and its applications," J. Sound Vib. **25**, 111–128 (1972).
34. M. Charnotskii, "Intensity fluctuations of flat-topped beam in non-Kolmogorov weak turbulence: comment," J. Opt. Soc. Am. A **29**, 1838–1840 (2012).
35. M. Charnotskii, "Comparison of four techniques for turbulent phase screens simulation," J. Opt. Soc. Am. A **37**, 738–747 (2020).
36. C. R. Dietrich and G. N. Newsam, "Fast and exact simulation of stationary Gaussian processes through circulant embedding of the covariance matrix," SIAM J. Sci. Comput. **18**, 1088–1107 (1997).
37. M. Cubillos and K. Luna, "Sinc method for generating and extending phase screens of atmospheric turbulence," J. Opt. Soc. Am. A **41**, 59–72 (2024).
38. J. P. Chilés and P. Delfiner, *Geostatistics: Modeling Spatial Uncertainty* (Wiley, 2012).
39. I. G. Graham, F. Y. Kuo, D. Nuyens, *et al.*, "Sloan analysis of circulant embedding methods for sampling stationary random fields," SIAM J. Numer. Anal. **56**, 1871–1895 (2018).
40. J. Schmidt, *Numerical Simulation of Optical Wave Propagation with Examples in Matlab* (SPIE, 2010).

41. R. J. LeVeque and J. Oliger, “Numerical methods based on additive splittings for hyperbolic partial differential equations,” Math. Comput. **40**, 469–497 (1983).
42. G. Strang, “On the construction and comparison of difference schemes,” SIAM J. Numer. Anal. **5**, 506–517 (1968).
43. T. Jahnke and C. Lubich, “Error bounds for exponential operator splittings,” BIT Numer. Math. **40**, 735–744 (2000).
44. D. L. Knepp, “Multiple phase-screen calculation of the temporal behavior of stochastic waves,” Proc. IEEE **71**, 722–737 (1983).
45. J. M. Martin and S. M. Flatté, “Intensity images and statistics from numerical simulation of wave propagation in 3-D random media,” Appl. Opt. **27**, 2111–2126 (1988).
46. V. P. Kandidov, “Monte-Carlo method in nonlinear statistical optics,” Usp. Fiz. Nauk **166**, 1309–1338 (1996).
47. A. Dembo, C. L. Mallows, and L. A. Shepp, “Embedding nonnegative definite Toeplitz matrices in nonnegative definite circulant matrices, with application to covariance estimation,” IEEE Trans. Inf. Theory **35**, 1206–1212 (2002).
48. M. Bachmayr, I. G. Graham, V. K. Nguyen, *et al.*, “Scheichl unified analysis of periodization-based sampling methods for Matérn covariances,” SIAM J. Numer. Anal. **58**, 2953–2980 (2020).
49. T. Gneiting, H. Ševčiková, D. B. Percival, *et al.*, “Fast and exact simulation of large Gaussian lattice systems in R^2: exploring the limits,” J. Comput. Graph. Stat. **15**, 483–501 (2006).
50. H. Helgason, V. Pipiras, and P. Abry, “Smoothing windows for the synthesis of Gaussian stationary random fields using circulant matrix embedding,” J. Comput. Graph. Stat. **23**, 616–635 (2014).
51. H. Helgason, S. Kechagias, and V. Pipiras, “Convex optimization and feasible circulant matrix embeddings in synthesis of stationary Gaussian fields,” J. Comput. Graph. Stat. **25**, 1158–1175 (2016).
52. O. Korotkova and I. Toselli, “Non-classic atmospheric optical turbulence,” Appl. Sci. **11**, 8487 (2021).
53. O. Korotkova, N. Farwell, and E. Shchepakina, “Light scintillation in oceanic turbulence,” Waves Random Complex Media **22**, 260–266 (2012).
54. V. A. Kulikov, “Estimation of turbulent parameters based on the intensity scintillations of the laser beam propagated through a turbulent water layer,” J. Appl. Phys. **119**, 123103 (2016).